# NUMERICAL SIMULATIONS OF ACTIVE FLOW CONTROL FOR ROTOR VIBRATION REDUCTION AT MODERATE TO HIGH ADVANCE RATIOS

Ryan P. Patterson* and Peretz P. Friedmann†
rppat@umich.edu peretzf@umich.edu
Department of Aerospace Engineering, University of Michigan, Ann Arbor, MI, USA 48109-2140

**Abstract**
The vibration reduction capability of active flow control (AFC) jets installed on the blades of a helicopter rotor is examined using comprehensive aeroelastic simulations. The simulations represent a four-blade hingeless rotor operating at several different advance ratios in the range of $0.20 \leq \mu \leq 0.35$. The closed-loop control scheme for reducing vibrations is based on the higher-harmonic control (HHC) algorithm, subject to actuator saturation constraints. Dynamic stall strongly influences vibrations at $\mu = 0.35$. Furthermore, the control sensitivity matrix used in the HHC algorithm varies significantly depending on the advance ratio. This produces different weightings of the 2-, 3-, 4-, and 5/Rev control harmonics used for vibration reduction. The overall level of vibrations at the rotor hub is consistently reduced by 70% to 80% below the baseline for all advance ratios considered. The reduction of in-plane shear force vibrations improves as the advance ratio increases, indicating that the adverse effects of dynamic stall are alleviated by AFC. The performance penalty associated with vibration reduction is also calculated. The additional rotor power required increases with advance ratio, due to increased drag penalty associated with fluidic actuation.

## NOTATION

| | |
|---|---|
| $\mathbf{A}, \mathbf{B}, \mathbf{C}$ | Coefficient matrices defined for flow control ROM |
| $b$ | Rotor blade semi-chord length |
| $c$ | Rotor blade chord length |
| $C_l, C_m, C_d$ | Sectional lift, moment, and drag coefficients |
| $C_{df}$ | Helicopter fuselage drag coefficient |
| $C_T$ | Helicopter thrust coefficient |
| $C_W$ | Helicopter weight coefficient |
| $C_\mu$ | Jet momentum coefficient |
| $e$ | Blade root offset from the center of rotation |
| $EI_{\eta\eta}, EI_{\zeta\zeta}$ | Principal bending stiffness of the blade cross-section |
| $f$ | Equivalent flat plate area of the helicopter fuselage |
| $\Delta\mathbf{f}$ | Vector of aerodynamic loads predicted by flow control ROM |
| $F_{x4}, F_{y4}, F_{z4}$ | 4/Rev components of hub shear |
| $GJ_b$ | Torsional stiffness of the blade cross-section |
| $I_{MB2}, I_{MB3}$ | Principal mass moments of inertia of the blade cross-section |
| $J$ | Quadratic cost function for HHC algorithm |
| $K$ | Static gain associated with process model |
| $L_b$ | Blade length |
| $\dot{m}_{\text{jet}}$ | Flow control jet mass flow rate |
| $M$ | Local Mach number |
| $M_b$ | Blade mass |
| $M_{\text{jet}}$ | Flow control jet Mach number |
| $M_{x4}, M_{y4}, M_{z4}$ | 4/Rev components of hub moment |
| $N_b$ | Number of rotor blades |
| $p_{o,\text{jet}}$ | Flow control jet stagnation pressure |
| $P_{\text{jet}}$ | Flow control jet power |
| $\mathbf{Q}$ | Aerodynamic transfer matrix |
| $\tilde{\mathbf{Q}}$ | Approximation of $\mathbf{Q}$ |
| $\mathbf{Q_z}$ | Weighting matrix on the vibratory hub loads |
| $R$ | Rotor blade radius |
| $\mathbf{R}$ | Weighting matrix on the control input |
| $s$ | Laplace variable |
| $\bar{s}$ | Nondimensional Laplace variable |
| $t$ | Dimensional time |
| $\bar{t}$ | Reduced time |
| $\mathbf{T}$ | Sensitivity matrix relating control input to the plant output |
| $u_{cont}$ | Continuous flow control input signal |
| $u^{\text{SS}}, u^{\text{PS}}$ | Suction side and pressure side flow control inputs |
| $\mathbf{u}$ | Control input vector |
| $\mathbf{u}_{\text{fc}}$ | Vector of flow control inputs |
| $U$ | Local oncoming flow velocity magnitude |
| $U_{\text{jet}}$ | Flow control jet velocity magnitude |
| $w_{\text{jet}}$ | Chordwise width of flow control jet orifice on airfoil surface |

* Ph.D. Candidate
† François-Xavier Bagnoud Professor

***Copyright Statement***
*The authors confirm that they, and/or their company or organization,* hold *copyright on all of the original material included in this paper. The authors also confirm that they have obtained permission, from the copyright holder of any third party material included in this paper, to publish it as part of their paper. The authors confirm that they give permission, or have obtained permission from the copyright holder of this paper, for the publication and distribution of this paper and recorded presentations as part of the ERF proceedings or as individual offprints from the proceedings and for inclusion in a freely accessible web-based repository.*

Presented at 47th European Rotorcraft Forum, United Kingdom, 7-9th September, 2021.
*This work is licensed under the Creative Commons Attribution International License (CC BY). Copyright © 2021 by author(s).*

| | |
|---|---|
| $\mathbf{x}_{\mathrm{fc}}$ | Vector of flow control ROM states |
| $X_A$ | Offset between the aerodynamic center and the elastic axis |
| $X_{FA}, Z_{FA}$ | Longitudinal and vertical offsets between rotor hub and helicopter aerodynamic center |
| $X_{FC}, Z_{FC}$ | Longitudinal and vertical offsets between rotor hub and helicopter center of gravity |
| $X_{Ib}$ | Offset of the blade cross-sectional center of mass from the elastic axis |
| $X_{IIb}$ | Offset of the blade cross-sectional center of area from the elastic axis |
| $X_t, Z_t$ | Longitudinal and vertical offsets between the tail rotor and the rotor hub center |
| $\mathbf{z}$ | Plant output vector |
| $\alpha$ | Angle of attack |
| $\beta_p$ | Blade precone angle |
| $\gamma$ | Lock number |
| $\theta_0, \theta_{1c}, \theta_{1s}$ | Collective and cyclic pitch settings |
| $\theta_{tw}$ | Blade pretwist distribution |
| $\mu$ | Helicopter advance ratio |
| $\sigma$ | Rotor solidity |
| $\tau$ | Time constant associated with process model |
| $\psi$ | Azimuth angle |
| $\omega_F, \omega_L, \omega_T$ | Blade flap, lag, and torsional natural frequencies |
| $\Omega$ | Rotor angular speed |

## 1. INTRODUCTION, BACKGROUND, AND OBJECTIVES

The vibratory loads generated on a helicopter rotor are primarily due to the coupled aeroelastic response of the blades as a result of unsteady aerodynamic interactions. In low-speed descending conditions, high vibration levels are associated with blade-vortex interaction (BVI), which involves a highly complex wake structure. High vibration levels are also experienced in high-speed conditions where dynamic stall occurs. This involves unsteady flow separation and reattachment producing large variations in angle of attack. Vibrations have an adverse effect on the fatigue life of the blades, as well as other mechanical and electronic components, and thus affect maintenance and operating costs. Vibration levels also have an influence on passenger comfort. Therefore, reduction of vibratory loads is a critical consideration in rotorcraft design.

A review of active vibration control approaches was presented in Ref. [1], emphasizing the use of on-blade control effectors to reduce vibrations at the source. The advantage of on-blade control, compared to higher-harmonic control (HHC) implemented at the swashplate or pitch-link actuated individual blade control, is the relatively low power penalty required for actuation. Partial-span trailing edge flaps are the most mature type of actuators considered for on-blade control, since these have been studied in aeroelastic simulations [2-4], wind tunnel tests on Mach-scaled [5] and full-scale [6] rotors, and flight tests [7]. Microflaps have also been studied extensively in CFD simulations [8] and aeroelastic simulations [9-11] for vibration reduction.

The feasibility of on-blade active flow control (AFC) as an alternative to electromechanical actuation has been demonstrated in recent numerical simulations. A CFD model of the fluidic actuators was developed in Ref. [12] to characterize the actuator performance in static and dynamic situations resembling the rotor environment. The static airfoil simulations were validated using experimental data from earlier wind tunnel experiments [13-14]. Subsequently, a CFD-based reduced-order model (ROM) for calculating unsteady aerodynamic loads at reduced computational cost was developed in Ref. [15]. The ROM exhibits close agreement with full-order CFD predictions and reduces computer run time by four orders of magnitude. Most recently, the ROM was integrated with the comprehensive aeroelastic rotor simulation code AVINOR (**A**ctive **Vi**bration and **No**ise **R**eduction) for closed-loop vibration reduction [16]. Open-loop and closed-loop control simulations revealed that the vibration levels evaluated at the hub of a four-bladed hingeless rotor are most sensitive to actuation at the 4/Rev frequency. Furthermore, the vibration reduction achieved using AFC was comparable to that of a microflap, including a similar performance penalty due to drag. The potential advantage of AFC compared to a microflap is the elimination of moving parts.

The HHC algorithm has been implemented for closed-loop, on-blade control simulations involving actively controlled trailing edge flaps [2,3,17], microflaps [9-10], and recently AFC [16] for vibration reduction. The HHC algorithm was examined from a control theory perspective in Ref. [17]. Convergence and stability characteristics were analyzed for three versions of the algorithm, including the classical invariant version, an adaptive version, and a relaxed version. The adaptive version of HHC is appropriate for situations involving nonlinear phenomena such as BVI or dynamic stall. The effect of imposing saturation constraints on the control amplitude during HHC was examined in Refs. [10,18,19].

The main objective of this paper is to demonstrate the vibratory load reduction capability of AFC using closed-loop aeroelastic simulations. The specific objectives are:

1. Examination of the vibratory loads produced with and without AFC at various advance ratios in the range of $0.20 \leq \mu \leq 0.35$.
2. Examination of the control sensitivity matrix used by the HHC algorithm for closed-loop


*This work is licensed under the Creative Commons Attribution International License (CC BY). Copyright © 2021 by author(s).*

vibration control and its dependence on the rotor advance ratio.

3. Calculation of the rotor performance penalty associated with vibratory loads reduction.

To illustrate the vibration reduction capability of AFC under various flow conditions, four different advance ratios are examined: $\mu = 0.20, 0.25, 0.30$, and $0.35$. The low-speed cases are relatively benign. However, the high-speed case of $\mu = 0.35$ is more challenging to model, since dynamic stall has a significant effect on vibratory loads.

## 2. BI-DIRECTIONAL FLUIDIC ACTUATION

The flow control device, depicted in Fig. 1, is a recently developed configuration that has been tested in wind tunnel experiments at Georgia Tech [13]. A CFD simulation approach for modeling the actuators was developed in Ref. [12] and was validated using wind tunnel data. The device consists of two pulsed fluidic actuators, installed near the trailing edge of a VR-12 airfoil model on the suction side (SS) and pressure side (PS). The SS and PS actuators are controlled independently, and each have two operating modes: tangential blowing and normal blowing. Note that the "normal" blowing mode refers to a jet that is oriented upstream at an angle of $60°$ relative to the airfoil chord line. The tangential and normal blowing outlets on the airfoil surface are located $0.84c$ and $0.88c$ from the leading edge of the airfoil, respectively.

In practice, an internal fluidic switching mechanism is used to select the operating mode for each actuator, i.e., tangential blowing, normal blowing, or off. A steady supply of air, provided by an air compression system, is channeled through an internal system of ducts within the airfoil, shown in Fig. 1. The steady supply jet is diverted to the appropriate output channel by control jets within each actuator. Furthermore, the operating modes can be rapidly switched, or pulsed, to produce alternating and intermittent actuation signals.

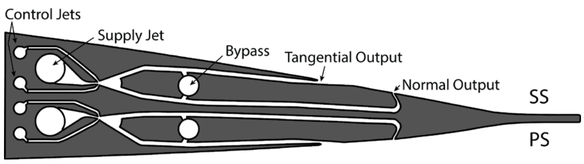


Figure 1. Internal details of trailing edge fluidic actuators for SS and PS blowing on a tabbed VR-12 airfoil

## 3. COMPUTATIONAL MODELING APPROACH

The complex unsteady flow phenomena introduced by fluidic actuation requires a CFD-based approach for accurate calculation of aerodynamic loads. However, the excessive computational cost of CFD simulations precludes their use in active vibration control simulations. Therefore, a reduced-order model (ROM) based on data obtained from unsteady Reynolds-averaged Navier-Stokes (URANS) simulations is employed, to represent the aerodynamic loads induced by AFC. The ROM provides a four order of magnitude reduction in computer run time compared to CFD. A detailed description of the CFD-based ROM was presented in Ref. [15]. The essential features of the ROM approach are presented next. Additionally, the integration of the ROM into the AVINOR aeroelastic code is also briefly described.

### 3.1. CFD Simulation Approach

The CFD simulation approach is based on a simplified model of the flow control actuators. The fluidic switching mechanism described in the previous section is not modeled in the CFD simulations. Instead, the tangential and normal blowing modes are approximated by prescribing inflow conditions at the boundaries shown in Fig. 2.

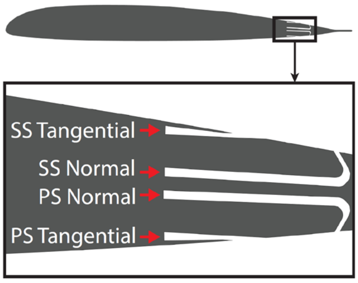


Figure 2. VR-12 airfoil and details of simplified fluidic actuator geometry

The strength of actuation is characterized by a jet momentum coefficient, defined as:

$$C_\mu = \frac{\rho_{\text{jet}} U_{\text{jet}}^2 w_{\text{jet}}}{\rho_\infty U_\infty^2 c} \tag{1}$$

The coefficient $C_\mu$ is a measure of the relative jet strength, and it represents the ratio of the momentum injected by the jet to the momentum of the freestream flow. For a given $C_\mu$, the inflow boundary conditions in the simulations are prescribed based on the maximum velocity of the jet issuing from the airfoil surface, $U_{\text{jet}}$. Specifically, the jet Mach number, $M_{\text{jet}}$, is used to determine the stagnation pressure of the jet, $p_{o,\text{jet}}$, from isentropic relations:

$$\frac{p_{o,\text{jet}}}{p_\infty} = \left(1 + \frac{\gamma - 1}{2} M_{\text{jet}}^2\right)^{\gamma/(\gamma-1)} \tag{2}$$

where $p_\infty$ is the freestream static pressure and $\gamma = 1.4$ for air. When one of the jets is active, the stagnation pressure at the corresponding inlet boundary is


*This work is licensed under the Creative Commons Attribution International License (CC BY). Copyright © 2021 by author(s).*

prescribed as $p_{o,\mathrm{jet}}$. Otherwise, the inlet boundary is treated as a wall boundary.

The computational domain for the 2D airfoil simulations is shown in Fig. 3. It is a structured C-grid composed of 108,000 quadrilateral elements with a far-field boundary 50 chord-lengths from the airfoil. A grid refinement study was performed in Ref. [12], to determine the appropriate grid spacing. The simulations are performed using the CFD++ code [20], a commercially available code developed and marketed by Metacomp Technologies. The Menter $k$-$\omega$ shear stress transport (SST) model is selected for the simulations, and a fully-turbulent boundary layer is assumed.

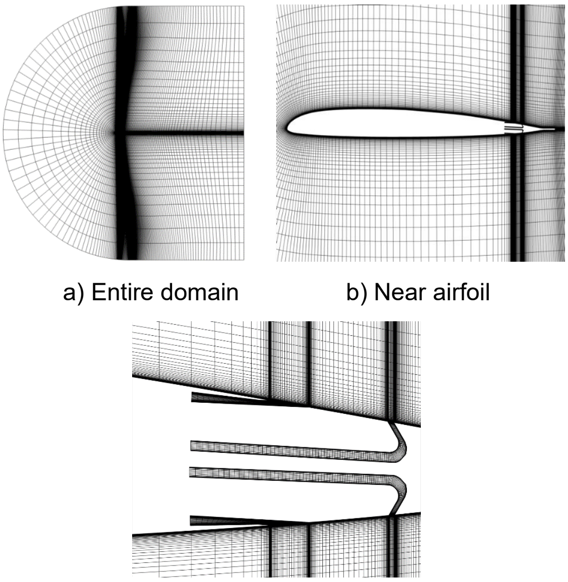

a) Entire domain b) Near airfoil

c) Near actuators

Figure 3. Structured computational grid for 2D CFD simulations of VR-12 airfoil with fluidic actuators

The modes of flow control considered are the SS and PS normal blowing modes. To simplify the current analysis, the tangential blowing modes are not included when performing vibration control. Thus, each actuator (SS and PS) has two possible operating states: normal blowing on or off.

### 3.2. Flow Control ROM Formulation

The ROM is formulated by treating the CFD simulation framework as a black box and applying a system identification procedure. From a high-level perspective, the black box maps the flow control input variables $\mathbf{u}_{\mathrm{fc}}(t)$ to the unsteady changes in aerodynamic loads $\Delta\mathbf{f}(t)$, where:

(3) $$\mathbf{u}_{\mathrm{fc}} = \begin{Bmatrix} u^{\mathrm{SS}} \\ u^{\mathrm{PS}} \end{Bmatrix} \text{ and } \Delta\mathbf{f} = \begin{Bmatrix} \Delta C_l \\ \Delta C_m \\ \Delta C_d \end{Bmatrix}$$

The operating states of the SS and PS jets are either on or off at a fixed jet strength, and thus $u^{\mathrm{SS}}$ and $u^{\mathrm{PS}}$ are each assigned a value of 1 or 0. An approximate mapping from inputs to outputs is formulated in the Laplace domain:

(4) $$\mathcal{L}[U(\bar{t})\Delta\mathbf{f}(\bar{t})] = \mathbf{Q}(\bar{s})\mathcal{L}[\mathbf{u}_{\mathrm{fc}}(\bar{t})]$$

where reduced time $\bar{t} = \frac{1}{b}\int_0^t U(\tau)\mathrm{d}\tau$, interpreted as the distance traveled by a rotor blade measured in semi-chords, is used in order to properly account for unsteady freestream effects. For rotary-wing applications, this definition of reduced time is more appropriate than the traditional definition used in fixed-wing applications, $\bar{t} = \frac{Ut}{b}$.

The aerodynamic transfer function $\mathbf{Q}(\bar{s})$ is a 3×2 matrix:

(5) $$\mathbf{Q}(\bar{s}) = \begin{bmatrix} Q_l^{\mathrm{SS}}(\bar{s}) & Q_l^{\mathrm{PS}}(\bar{s}) \\ Q_m^{\mathrm{SS}}(\bar{s}) & Q_m^{\mathrm{PS}}(\bar{s}) \\ Q_d^{\mathrm{SS}}(\bar{s}) & Q_d^{\mathrm{PS}}(\bar{s}) \end{bmatrix}$$

Each entry of the transfer matrix is approximated using a process model of the form

(6) $$\tilde{Q}(\bar{s}) = \frac{K}{1+\tau s}$$

The static gain, $K$, is interpreted in the time domain as the steady-state value of the output due to sustained steady blowing. The time constant, $\tau$, is associated with the rise time.

The process model form is transformed to the time domain using the inverse Laplace transform, which yields the state space model,

(7) $$\frac{\mathrm{d}\mathbf{x}_{\mathrm{fc}}}{\mathrm{d}t} = \frac{U(t)}{b}\left(\mathbf{A}\mathbf{x}_{\mathrm{fc}}(t) + \mathbf{B}\mathbf{u}_{\mathrm{fc}}(t)\right)$$

(8) $$\Delta\mathbf{f}(t) = \frac{1}{U(t)}\mathbf{C}\mathbf{x}_{\mathrm{fc}}(t)$$

where

(9) $$\mathbf{A} = \mathrm{diag}\left\{\frac{-1}{\tau_l^{\mathrm{SS}}}, \frac{-1}{\tau_l^{\mathrm{PS}}}, \frac{-1}{\tau_m^{\mathrm{SS}}}, \frac{-1}{\tau_m^{\mathrm{PS}}}, \frac{-1}{\tau_d^{\mathrm{SS}}}, \frac{-1}{\tau_d^{\mathrm{PS}}}\right\}$$

(10) $$\mathbf{B} = \begin{bmatrix} \mathbf{I}_2 \\ \mathbf{I}_2 \\ \mathbf{I}_2 \end{bmatrix}$$

(11) $$\mathbf{C} = \begin{bmatrix} \frac{K_l^{\mathrm{SS}}}{\tau_l^{\mathrm{SS}}} & \frac{K_l^{\mathrm{PS}}}{\tau_l^{\mathrm{PS}}} & 0 & 0 & 0 & 0 \\ 0 & 0 & \frac{K_m^{\mathrm{SS}}}{\tau_m^{\mathrm{SS}}} & \frac{K_m^{\mathrm{PS}}}{\tau_m^{\mathrm{PS}}} & 0 & 0 \\ 0 & 0 & 0 & 0 & \frac{K_d^{\mathrm{SS}}}{\tau_d^{\mathrm{SS}}} & \frac{K_d^{\mathrm{PS}}}{\tau_d^{\mathrm{PS}}} \end{bmatrix}$$

and $\mathbf{I}_2$ denotes a 2×2 identity matrix. Note that the relation $\frac{\mathrm{d}}{\mathrm{d}\bar{t}} = \frac{b}{U(t)}\frac{\mathrm{d}}{\mathrm{d}t}$ can be used to switch between the independent variables $t$ and $\bar{t}$.


*This work is licensed under the Creative Commons Attribution International License (CC BY). Copyright © 2021 by author(s).*

To account for the ranges of Mach number and angle of attack encountered on a helicopter rotor, a model scheduling approach resembling the CFD-based RFA [9] is used. In this formulation, Eqs. (7) and (8) are modified by allowing the coefficient matrices, $\mathbf{A}$ and $\mathbf{C}$, to vary with $M$ and $\alpha$. The resulting state space model in the time domain is written as

(12) $$\frac{\mathrm{d}\mathbf{x}_{\mathrm{fc}}}{\mathrm{d}t} = \frac{U(t)}{b}\left(\mathbf{A}(M,\alpha)\mathbf{x}_{\mathrm{fc}}(t) + \mathbf{B}\mathbf{u}_{\mathrm{fc}}(t)\right)$$

(13) $$\Delta\mathbf{f}(t) = \frac{1}{U(t)}\mathbf{C}(M,\alpha)\mathbf{x}_{\mathrm{fc}}(t)$$

In Eqs. (12) and (13), the coefficient matrices $\mathbf{A}(M,\alpha)$ and $\mathbf{C}(M,\alpha)$ are evaluated at intermediate flow conditions that occur between the training cases by using Kriging interpolation [21]. Kriging is a nonlinear approach capable of handling complex multi-dimensional functions based on limited training data sets. It is also non-parametric, meaning that no fixed structure is assumed and all training points are used in the prediction. The ROM approach was validated in Ref. [15] for unsteady PS/SS actuation on a pitching/plunging airfoil with sinusoidally-varying freestream Mach number, representing rotor blade vibrations at 75% span. The ROM predictions showed close agreement with direct CFD simulations. The advantage of using the ROM is the substantial reduction in computer run time. The ROM run time is 5.5 seconds on a conventional laptop PC, compared to a CFD run time of 63 hours on 8 high-performance cores. This represents a reduction in computer run time by more than four orders of magnitude. This reduction in computational cost is required so as to enable active control simulations in a comprehensive code such as AVINOR.

## 3.3. Aeroelastic Simulations Using the AVINOR Code

Active control simulations are performed using the comprehensive rotorcraft aeroelastic code AVINOR. The code was developed at the University of Michigan to analyze the aeroelastic response and stability of helicopter rotors in forward flight, and it has been validated in numerous previous studies [2,3,22,23]. The code includes the capability to model actively controlled trailing edge flaps and microflaps integrated into the rotor blades. The code also features a higher-harmonic control (HHC) algorithm, which can be used to perform closed-loop simulations aimed at vibratory load or acoustic noise reduction. The ROM described in the previous section is incorporated into AVINOR to model the unsteady aerodynamic effects induced by flow control on the rotor blades. A complete description of the most recent version of AVINOR is found in Ref. [23]. For convenience, the relevant components of the code are summarized.

### 3.3.1 Structural Dynamic Model

The structural dynamic model is geometrically nonlinear, to account for moderate blade deflections, and represents the fully coupled flap-lag-torsional dynamics of each blade. The equations of motion are approximated using a Galerkin formulation that includes three flap, two lead-lag, and two torsional vibration modes of the rotating blades. The rotor model used resembles an MBB BO-105 four-bladed hingeless soft-in-plane rotor.

### 3.3.2 Aerodynamic Model

Unsteady aerodynamic loads in attached flow are calculated at several stations along the blades using the CFD-based RFA model [9]. This 2D compressible unsteady aerodynamic model is linked to a 3D free-wake model, developed in Ref. [2], which produces a spanwise and azimuthally varying inflow velocity distribution over the rotor. For the separated flow regime, the 2D loads are obtained from the ONERA dynamic stall model, which was implemented in Ref. [2].

The flow control ROM is incorporated into AVINOR such that it is directly compatible with the existing aerodynamic model. The unsteady changes in 2D lift, moment, and drag coefficients on the blade sections where the actuators are present are obtained from the ROM, which modifies the 2D sectional loads obtained from the CFD-based RFA model.

### 3.3.3 Coupled Aeroelastic Response and Rotor Trim Solution

The combined structural and aerodynamic equations represent a system of coupled non-linear ordinary differential equations in state-variable form. A propulsive trim procedure is employed to enforce the equilibrium of three force equations (longitudinal, lateral, and vertical) and three moment equations (roll, pitch, and yaw), representing a helicopter in free flight. A simplified tail rotor model, based on uniform inflow and blade element theory, is used. The required trim variables are obtained from the trim procedure. The trim variables are: the rotor shaft angle $\alpha_R$; the collective and cyclic pitch settings $\theta_0$, $\theta_{1s}$, and $\theta_{1c}$; the roll angle $\phi_R$; and the tail rotor constant pitch setting $\theta_{0t}$. The coupled system of equations is integrated in time using the DDEABM solver, which employs a variable-order, predictor-corrector-based Adams-Bashforth scheme.

## 4. HIGHER HARMONIC CONTROL ALGORITHM

The higher-harmonic control (HHC) algorithm has been used extensively for active control of vibrations and acoustic noise in rotorcraft [1]. The algorithm is


*This work is licensed under the Creative Commons Attribution International License (CC BY). Copyright © 2021 by author(s).*

a frequency-domain approach based on the assumption that the helicopter can be represented by a linear model relating the output $\mathbf{z}$ to the input $\mathbf{u}$. The approach is applied to disturbances (vibrations or noise) having known frequency content that is predominantly $N_b$/Rev, where $N_b$ is the number of blades. When performing vibration reduction on a four-blade rotor, the output $\mathbf{z}$ consists of the 4/Rev vibratory loads and the input vector $\mathbf{u}$ includes harmonic control inputs at the 2-, 3-, 4-, and 5/Rev frequencies.

The HHC algorithm is designed for steady trimmed flight conditions. The measurement of the plant output and update of the control input are performed at specific times, $t = k\tau$, where $\tau$ is the time interval between updates during which the plant output reaches a steady state. This time interval can be one or more revolutions. For the present simulations, six revolutions are sufficient to achieve a steady-state (converged) condition after applying the control update.

With the introduction of a disturbance $\mathbf{w}$, representing the helicopter operating condition, the plant output at the $k$th time step is given by

(14) $$\mathbf{z}_k = \mathbf{T}\mathbf{u}_k + \mathbf{W}\mathbf{w}$$

where the sensitivity matrix $\mathbf{T}$ represents the linear approximation of the helicopter response to the control and is given by

(15) $$\mathbf{T} = \frac{\partial \mathbf{z}}{\partial \mathbf{u}}$$

At the initial condition, $k = 0$:

(16) $$\mathbf{z}_0 = \mathbf{T}\mathbf{u}_0 + \mathbf{W}\mathbf{w}$$

Subtracting Eq. (16) from Eq. (14) to eliminate the unknown $\mathbf{w}$ yields

(17) $$\mathbf{z}_k = \mathbf{z}_0 + \mathbf{T}(\mathbf{u}_k - \mathbf{u}_0)$$

The controller is based on the minimization of a quadratic cost function:

(18) $$J(\mathbf{z}_k, \mathbf{u}_k) = \mathbf{z}_k^T\mathbf{Q}_\mathbf{z}\mathbf{z}_k + \mathbf{u}_k^T\mathbf{R}\mathbf{u}_k$$

The optimal control law is determined from the requirement

(19) $$\frac{\partial J(\mathbf{z}_k, \mathbf{u}_k)}{\partial \mathbf{u}_k} = 0$$

which yields the optimal control input, $\mathbf{u}_{k,\mathrm{opt}}$, given by

(20) $$\mathbf{u}_{k,\mathrm{opt}} = -(\mathbf{T}^T\mathbf{Q}_\mathbf{z}\mathbf{T} + \mathbf{R})^{-1}(\mathbf{T}^T\mathbf{Q}_\mathbf{z})(\mathbf{z}_0 - \mathbf{T}\mathbf{u}_0)$$

This is the classical version of the HHC algorithm, which yields an explicit relation for the optimal control input. In this formulation, the sensitivity matrix $\mathbf{T}$ is assumed to be invariant. Furthermore, the $\mathbf{T}$ matrix can be identified offline, using open-loop control signals, before performing closed-loop control.

When non-linearities in the helicopter response are significant, such as during heavy blade-vortex interaction (BVI) or dynamic stall conditions, an invariant $\mathbf{T}$ matrix produces a poor approximation of the helicopter response. Under such conditions, it is more appropriate to use an adaptive version of the HHC algorithm, where $\mathbf{T}$ is updated using least-squares methods after every control update [17]. To describe the adaptive HHC algorithm, relative output and input vectors are defined, $\Delta\mathbf{z}_k$ with length $2p$ and $\Delta\mathbf{u}_k$ with length $2m$ as

(21) $$\Delta\mathbf{z}_k = \mathbf{z}_k - \mathbf{z}_{k-1}, \;\; \Delta\mathbf{u}_k = \mathbf{u}_k - \mathbf{u}_{k-1}$$

and $\Delta\mathbf{Z}_k$ of size $2p \times k$ and $\Delta\mathbf{U}_k$ of size $2m \times k$ as

(22) $$\Delta\mathbf{Z}_k = [\Delta\mathbf{z}_1 \cdots \Delta\mathbf{z}_k], \;\; \Delta\mathbf{U}_k = [\Delta\mathbf{u}_1 \cdots \Delta\mathbf{u}_k]$$

Hence,

(23) $$\Delta\mathbf{Z}_k = \mathbf{T}\Delta\mathbf{U}_k$$

Assuming $\Delta\mathbf{U}_k\Delta\mathbf{U}_k^T$ is non-singular, one can define

(24) $$\mathbf{P}_k = (\Delta\mathbf{U}_k\Delta\mathbf{U}_k^T)^{-1}$$

and from Eq. (23) the least-squares estimate $\hat{\mathbf{T}}_{\mathrm{LS}_k}$ of $\mathbf{T}$ is given by

(25) $$\hat{\mathbf{T}}_{\mathrm{LS}_k} = \Delta\mathbf{Z}_k\Delta\mathbf{U}_k^T\mathbf{P}_k$$

The recursive least-squares method is used to iteratively update $\hat{\mathbf{T}}_{\mathrm{LS}_k}$ based on the past and current values of $\Delta\mathbf{z}_k$ and $\Delta\mathbf{u}_k$. The updated estimate $\hat{\mathbf{T}}_{\mathrm{LS}_k}$ is used at each control update step to calculate the optimal control input $\mathbf{u}_{k,\mathrm{opt}}$ as follows:

(26) $$\mathbf{u}_{k,\mathrm{opt}} = -\left(\hat{\mathbf{T}}_{\mathrm{LS}_k}^T\mathbf{Q}_\mathbf{z}\hat{\mathbf{T}}_{\mathrm{LS}_k} + \mathbf{R}\right)^{-1}\left(\hat{\mathbf{T}}_{\mathrm{LS}_k}\mathbf{Q}_\mathbf{z}\right)\left(\mathbf{z}_0 - \hat{\mathbf{T}}_{\mathrm{LS}_k}\mathbf{u}_0\right)$$

The adaptive HHC algorithm has been shown to perform better than the classical HHC when reducing vibrations encountered during heavy BVI conditions [17]. The conditions corresponded to an advance ratio of $\mu = 0.15$ and a descent angle of $6.5°$. Since most of the conditions examined in the present study are not severely impacted by non-linear phenomena like BVI or dynamic stall, the classical version of the HHC algorithm can be used. The classical HHC is used for vibration reduction in the range of $0.20 \leq \mu \leq 0.30$. An additional high-speed case is considered at $\mu = 0.35$. In this case, dynamic stall affects the vibratory loads and introduces nonlinear effects into the helicopter response. Therefore, the adaptive HHC is employed for the case of $\mu = 0.35$. The classical and adaptive versions of HHC yield nearly identical results for the more benign cases of $0.20 \leq \mu \leq$

Presented at 47th European Rotorcraft Forum, United Kingdom, 7-9th September, 2021.
*This work is licensed under the Creative Commons Attribution International License (CC BY). Copyright © 2021 by author(s).*

$0.30$. In all cases, after the optimal control input is calculated, the rotor is re-trimmed in AVINOR to maintain a steady flight condition.

### 4.1. HHC Implementation for AFC

A continuous AFC input signal $u_{cont}$ is defined when implementing HHC. The signal is allowed to vary continuously between two actuation limits, which are full-strength PS actuation ($u_{cont} = -1$) and full-strength SS actuation ($u_{cont} = 1$) where $u_{cont} = 0$ indicates both jets are off. The continuous signal is mapped to the two ROM input variables $u^{\mathrm{SS}}$ and $u^{\mathrm{PS}}$ in Eq. (3) as

$$u^{\mathrm{SS}} = \begin{cases} |u_{cont}|, & 0.01 \le u_{cont} \le 1 \\ 0, & u_{cont} < 0.01 \end{cases} \tag{27}$$

$$u^{\mathrm{PS}} = \begin{cases} 0, & u_{cont} > -0.01 \\ |u_{cont}|, & -1 \le u_{cont} \le -0.01 \end{cases} \tag{28}$$

Note that while one jet is on, the other jet is off. Both jets are turned off below 1% jet strength, since AFC at this strength has a negligible effect on aerodynamic loads. By using a continuous actuation signal, superposition of the 2-, 3-, 4-, and 5/Rev harmonics for HHC is expressed as

$$u_{cont}(\psi, \mathbf{u}_k) = \sum_{N=2}^{5} [u_{Nc} \cos N\psi + u_{Ns} \sin N\psi] \tag{29}$$

The control input vector $\mathbf{u}_k$ determined by the HHC algorithm is given by the cosine and sine amplitudes of the control harmonics:

$$\mathbf{u}_k = \{u_{2c}\ u_{2s}\ u_{3c}\ u_{3s}\ u_{4c}\ u_{4s}\ u_{5c}\ u_{5s}\}^T \tag{30}$$

This continuous formulation is directly compatible with the existing HHC algorithm.

For vibration reduction on a four-blade rotor, the output vector $\mathbf{z}_k$ consists of the cosine and sine components of the 4/Rev vibratory shear forces and moments at the rotor hub:

$$\mathbf{z}_k = \begin{Bmatrix} F_{x4c} \\ F_{x4s} \\ F_{y4c} \\ F_{y4s} \\ F_{z4c} \\ F_{z4s} \\ M_{x4c} \\ M_{x4s} \\ M_{y4c} \\ M_{y4s} \\ M_{z4c} \\ M_{z4s} \end{Bmatrix} \tag{31}$$

The weighting matrix $\mathbf{Q_z}$ in the cost function in Eq. (18) is a diagonal matrix. The twelve diagonal terms of $\mathbf{Q_z}$ are weights corresponding to the various components of the vibratory hub shears (longitudinal, lateral, and vertical) and vibratory hub moments (roll, pitch, and yaw). All components are weighted equally in the present study.

### 4.2. Actuator Saturation

In a practical setting, there are limitations on any actuation system. For example, the deflection of a trailing edge flap or a microflap cannot exceed a certain maximum value. For an AFC system, the jet strength produced by the fluidic actuators is limited by the power available from the air compression system. This imposes a constraint on the optimal control input calculated by the HHC algorithm, and therefore has an effect on the vibration reduction capability of the control system.

An optimization approach, developed in Ref. [10], is employed to ensure the AFC jet strength does not exceed this saturation limit. The optimization approach restates the HHC algorithm as a constrained nonlinear optimization problem:

$$\min_{\mathbf{u}_k} J(\mathbf{z}_k, \mathbf{u}_k) = \mathbf{z}_k^T \mathbf{Q_z} \mathbf{z}_k + \mathbf{u}_k^T \mathbf{R} \mathbf{u}_k \tag{32}$$

$$\text{subject to } |u_{cont}(\psi, \mathbf{u}_k)| \le u_{limit} \tag{33}$$

The optimization problem is solved using a sequential programming routine available in the `fmincon` tool in MATLAB. The AVINOR code, which is written in Fortran, calls the MATLAB application as an external routine to calculate the updated control input $\mathbf{u}_k$. The nonlinear constraint on $u_{cont}(\psi, \mathbf{u}_k)$, given by Eq. (33), is enforced at every integer value of $\psi$ over the range $[0°\ 360°]$. After calculating $\mathbf{u}_k$, six rotor revolutions are simulated within the AVINOR code, to reach a steady-state condition, before performing the next control update $\mathbf{u}_{k+1}$.

## 5. RESULTS AND DISCUSSION

The vibration reduction capability of the closed-loop AFC approach is presented for a four-blade hingeless rotor operating in forward flight at advance ratios between $0.20 \le \mu \le 0.35$. The rotor resembles the MBB BO-105 rotor. The rotor parameters are summarized in Table 1 and are nondimensionalized using $M_b$, $R$, and $1/\Omega$ for mass, length, and time, respectively. The AFC actuators cover 12% span on each blade and are centered at the 75% span location, as depicted in Fig. 4.


*This work is licensed under the Creative Commons Attribution International License (CC BY). Copyright © 2021 by author(s).*

Table 1. Rotor parameters used in computations

| | |
|---|---|
| Dimensional Rotor Data | |
| $R = 4.91$ m | |
| $M_b = 27.35$ kg | |
| $\Omega = 425$ RPM | |
| Non-Dimensional Rotor Data | |
| $N_b = 4$ | $c = 0.05498R$ |
| $L_b = 1.0$ | $e = 0$ |
| $X_A = 0$ | $\beta_p = 2.5°$ |
| $X_{Ib} = 0$ | $X_{IIb} = 0$ |
| $I_{MB2} = 0$ | $I_{MB3} = 0.0004$ |
| $EI_{\eta\eta} = 0.0302$ | $EI_{\zeta\zeta} = 0.0105$ |
| $GJ_b = 0.0015$ | $\omega_{F1} = 1.124$ |
| $\omega_{F2} = 3.404$ | $\omega_{F3} = 7.606$ |
| $\omega_{L1} = 0.732$ | $\omega_{L2} = 4.458$ |
| $\omega_{T1} = 3.170$ | $\omega_{T2} = 9.079$ |
| $\gamma = 5.5$ | $\sigma = 0.07$ |
| $\theta_{tw} = -8°$ | |
| Non-Dimensional Tail Rotor Data | |
| $X_t = 1.20$ | $Z_t = 0$ |
| Helicopter Data | |
| $C_W = 0.005$ | $fC_{df} = 0.031$ |
| $X_{FA} = 0$ | $Z_{FA} = 0.3$ |
| $X_{FC} = 0$ | $Z_{FC} = 0.3$ |

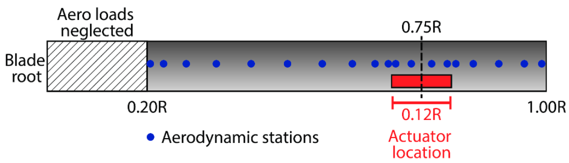

Figure 4. AFC-integrated rotor blade schematic for aeroelastic computations

### 5.1. Baseline Results Without Control

The baseline vibratory loads of the rotor without AFC are examined first. The vibratory loads at the rotor hub are calculated by integrating the distributed loads over the entire blade span in the rotating frame. Subsequently, the loads from each blade are transformed to the hub-fixed non-rotating frame, where the contributions from each blade are combined to yield the total hub shear forces and moments.

The various components of the 4/Rev hub loads are illustrated in Fig. 5 for advance ratios of $\mu = 0.20, 0.25, 0.30,$ and $0.35$. The low-speed cases of $\mu = 0.20$ and $\mu = 0.25$ are relatively benign cases to consider, since dynamic stall does not affect blade vibrations at these speeds. At $\mu = 0.35$, dynamic stall has a strong effect on the in-plane shear forces, as illustrated by the increased longitudinal and lateral shears. For the intermediate case of $\mu = 0.30$, dynamic stall is present, but to a lesser extent compared to $\mu = 0.35$. Moreover, the range of advance ratios considered encompasses a variety of different flow conditions for testing the vibration reduction potential of AFC.

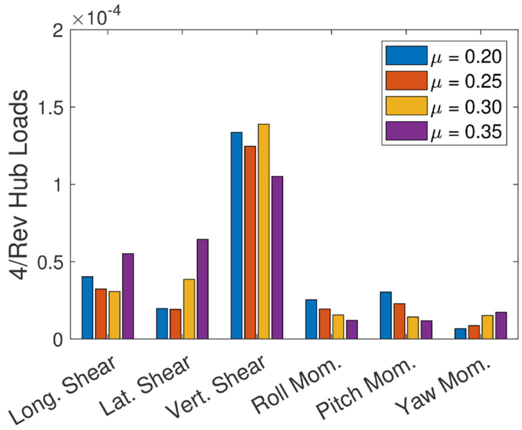

Figure 5. Baseline uncontrolled 4/Rev hub loads during trimmed level flight at various advance ratios; results are nondimensional

The propulsive trim procedure in AVINOR is used to determine the trim variable settings needed for steady level flight at each advance ratio. The effect of the advance ratio on each of the six trim variables in shown in Fig. 6. The rotor shaft angle increases linearly from $\alpha_R = 2.3°$ to $\alpha_R = 6.7°$ as the advance ratio increases from $\mu = 0.20$ to $\mu = 0.35$, since the forward thrust provided by the rotor must also increase. The collective pitch increases from $\theta_0 = 7°$ to $\theta_0 = 11°$, the longitudinal cyclic decreases from $\theta_{1s} = -3.7°$ to $\theta_{1s} = -7°$, and the lateral cyclic decreases from $\theta_{1c} = 0.9°$ to $\theta_{1c} = 0.3°$. The tail rotor pitch $\theta_{0t}$ and fuselage roll angle $\phi_R$ increase by 0.6° and 1.8°, respectively.

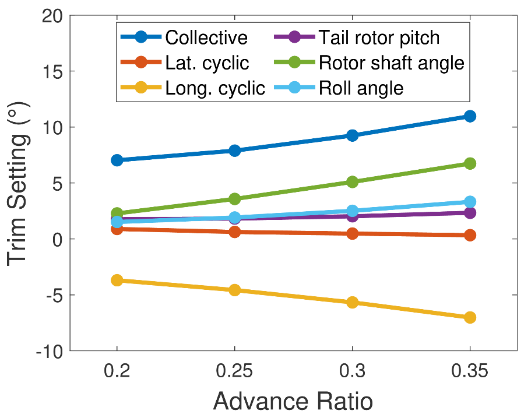

Figure 6. Trim variable settings for level flight at various advance ratios

### 5.2. Control Sensitivity Matrix for HHC

The control sensitivity matrix $\mathbf{T}$ used in the HHC algorithm is examined next. The matrix is defined in Eq. (15) and relates the output variables contained in $\mathbf{z}$ (the 4/Rev vibratory hub load components) to the input variables contained in $\mathbf{u}$ (the harmonic control


This work is licensed under the Creative Commons Attribution International License (CC BY). Copyright © 2021 by author(s).

inputs). Since there are 8 input variables and 12 output variables, $\mathbf{T}$ is an 8×12 matrix. The sensitivity matrix is constructed by perturbing the control inputs $\Delta\mathbf{u}$ and calculating the changes in vibratory loads $\Delta\mathbf{z}$ compared to the baseline without control. A period of six rotor revolutions is simulated after each perturbation, to ensure a converged solution.

There are a total of 96 unique entries in the $\mathbf{T}$ matrix. It is infeasible to examine how each of these entries varies with advance ratio $\mu$. However, it is convenient to express $\mathbf{T}$ as an array of several smaller 2×2 submatrices:

$$\mathbf{T} = \begin{bmatrix} \mathbf{T}_{2,F_{x4}} & \mathbf{T}_{2,F_{y4}} & \mathbf{T}_{2,F_{z4}} & \mathbf{T}_{2,M_{x4}} & \mathbf{T}_{2,M_{y4}} & \mathbf{T}_{2,M_{z4}} \\ \mathbf{T}_{3,F_{x4}} & \mathbf{T}_{3,F_{y4}} & \mathbf{T}_{3,F_{z4}} & \mathbf{T}_{3,M_{x4}} & \mathbf{T}_{3,M_{y4}} & \mathbf{T}_{3,M_{z4}} \\ \mathbf{T}_{4,F_{x4}} & \mathbf{T}_{4,F_{y4}} & \mathbf{T}_{4,F_{z4}} & \mathbf{T}_{4,M_{x4}} & \mathbf{T}_{4,M_{y4}} & \mathbf{T}_{4,M_{z4}} \\ \mathbf{T}_{5,F_{x4}} & \mathbf{T}_{5,F_{y4}} & \mathbf{T}_{5,F_{z4}} & \mathbf{T}_{5,M_{x4}} & \mathbf{T}_{5,M_{y4}} & \mathbf{T}_{5,M_{z4}} \end{bmatrix} \tag{34}$$

Each submatrix contains information relating the sine and cosine components of one input harmonic to the sine and cosine components of one hub load. For example, the submatrix relating 2/Rev actuation (consisting of the $u_{2c}$ and $u_{2s}$ inputs) to the 4/Rev longitudinal shear (consisting of the $F_{x4c}$ and $F_{x4s}$ outputs) is expressed as

$$\mathbf{T}_{2,F_{x4}} = \begin{bmatrix} \frac{\partial F_{x4c}}{\partial u_{2c}} & \frac{\partial F_{x4s}}{\partial u_{2c}} \\ \frac{\partial F_{x4c}}{\partial u_{2s}} & \frac{\partial F_{x4s}}{\partial u_{2s}} \end{bmatrix} \tag{35}$$

For the present analysis, the determinant of each 2×2 submatrix is calculated. This yields 24 pieces of information instead of 96. Although the individual sine and cosine components of the 2×2 submatrices provide information about the phase differences between inputs and outputs, the determinant of each submatrix is simpler to interpret. Each determinant provides an overall measure of the sensitivity between one input harmonic and the magnitude of one hub load component.

The effect of the advance ratio $\mu$ on each sensitivity determinant is illustrated in Fig. 7. Each plot shows the sensitivity of one hub load component as a function of $\mu$, where each line on the plot represents one control harmonic. The 4/Rev longitudinal and lateral shears (Figs. 7a and 7b) are most sensitive to 3/Rev actuation and become more sensitive as $\mu$ increases. The 3/Rev harmonic has the highest sensitivity because in-plane blade loads occurring at $N$/Rev are transmitted to the rotor hub as $(N-1)$/Rev and $(N+1)$/Rev harmonics. Since the four rotor blades are assumed to be identical in the simulations, only the 4/Rev harmonic of the hub loads is non-zero. Thus, the blade loads generated by 3/Rev actuation are transmitted to the rotor hub as 4/Rev in-plane vibrations. By contrast, vertical blade loads occurring at $N$/Rev are directly transmitted to the rotor hub at the $N$/Rev harmonic. Hence, for low advance ratios, the 4/Rev vertical shear force (Fig. 7c) is most sensitive to 4/Rev actuation. At higher advance ratios ($\mu \geq 0.30$), where dynamic stall is present, the vertical shear becomes more sensitive to 3/Rev actuation. The roll and pitching moments are most sensitive to

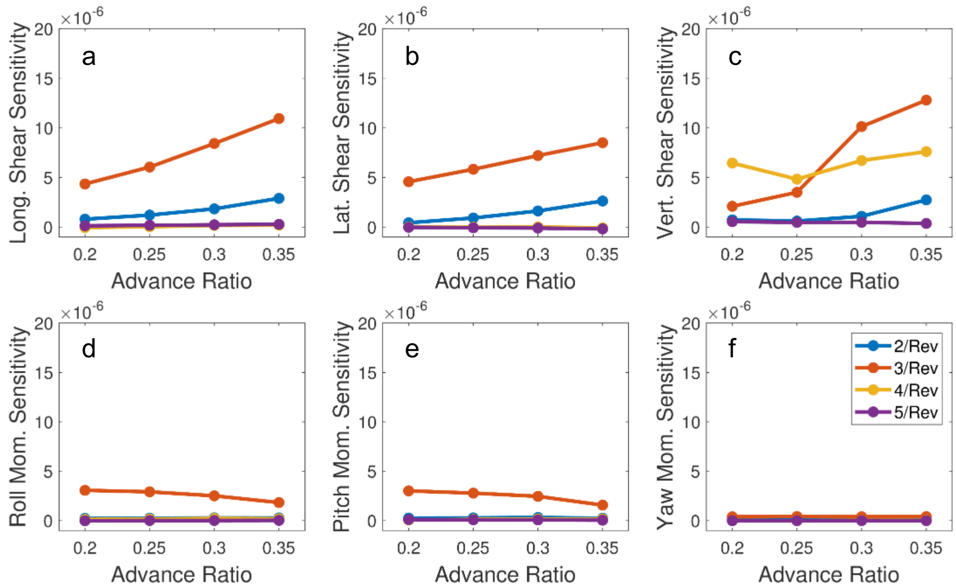


Figure 7. Variation of 4/Rev hub load sensitivies to AFC actuation applied at 2, 3, 4, and 5/Rev harmonics; results are nondimensional


*This work is licensed under the Creative Commons Attribution International License (CC BY). Copyright © 2021 by author(s).*

3/Rev actuation and become less sensitive as $\mu$ increases. The yaw moment vibrations are relatively insensitive to actuation at any frequency.

The control sensitivities provide some insight into the types of input signals that will be most effective for reducing vibrations when HHC is employed. Since the vertical shear force is the largest component of vibrations (Fig. 5), it is expected that the optimal control signals will be predominantly 4/Rev for lower advance ratios or 3/Rev for higher advance ratios.

### 5.3. Closed-Loop Vibration Control

The HHC approach is employed for closed-loop vibration control using AFC. The HHC algorithm is based on the minimization of the objective function $J$ in Eq. (18), which is a combination of the 4/Rev hub shears and moments. The optimal control signal is determined using the control sensitivity matrix $\mathbf{T}$, subject to actuator saturation constraints. As mentioned, the classical HHC algorithm uses an invariant $\mathbf{T}$ matrix that is identified offline prior to the closed-loop simulations. The adaptive HHC algorithm, however, uses a $\mathbf{T}$ matrix that is updated using a least-squares approach after each control update in the simulation. Adaptive HHC is needed for the high-speed case ($\mu = 0.35$) where dynamic stall significantly affects the prediction of vibratory loads. For the lower advance ratios, adaptive HHC produces nearly identical results as classical HHC, although at greater computational cost. Therefore, the classical HHC approach is used for $0.20 \leq \mu \leq 0.30$ and the adaptive HHC approach is used for $\mu = 0.35$.

For all simulations performed, the saturation limit for the AFC actuators was selected as $P_{\text{jet}} = 1.2$ kW/blade. Previous closed-loop simulations [16] performed at $\mu = 0.30$ indicated that this jet strength yields a good balance between vibration reduction and performance penalty, since larger saturation limits yield a diminishing level of improvement in vibrations with higher associated performance penalty.

Figure 8 illustrates the vibration reduction due to closed-loop AFC as a function of the advance ratio. For each of the hub load components, the baseline and controlled loads are compared. The vertical shear force is reduced by the greatest margin among the various hub load components: it is reduced by 81% to 86% below the baseline levels. Also, the controlled level of vertical shear vibrations is nearly constant across the range of advance ratios. This is an encouraging result which demonstrates the effectiveness of the AFC approach in a variety of flow conditions. Furthermore, the reduction of longitudinal and lateral shear vibrations improves as $\mu$ increases, indicating that the adverse effects of dynamic stall are alleviated by AFC.

The optimal control input signals computed by the HHC algorithm are compared in Fig. 9 for the four advance ratios. The signals are all predominantly 4/Rev, with minor variations due to superposition with other harmonics. In Fig. 10, the signals are decomposed in terms of the amplitude and phase of each harmonic (2-, 3-, 4-, and 5/Rev) as a function of $\mu$. The 4/Rev harmonic is consistently the largest component of the signals. The 4/Rev phase increases gradually from $136°$ to $178°$ as $\mu$ increases.

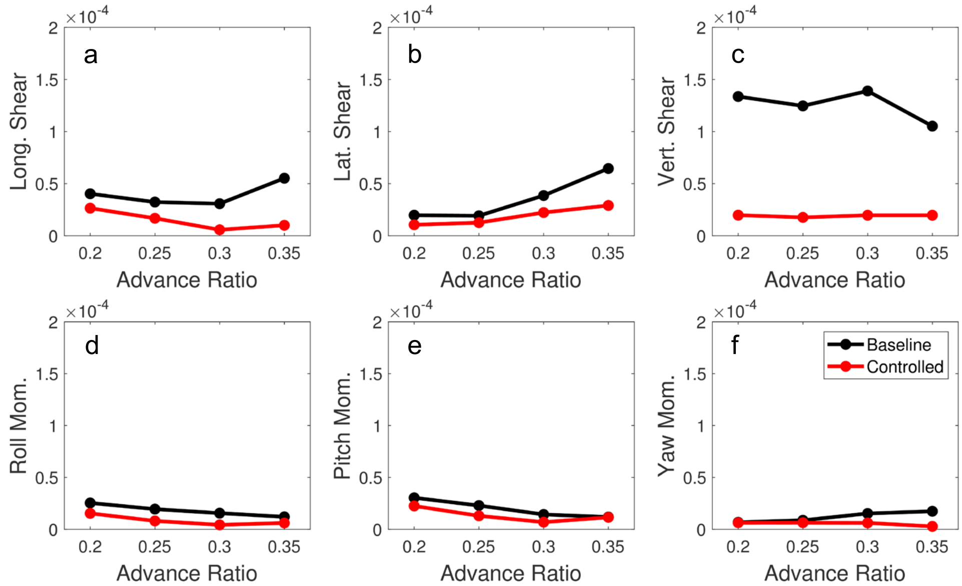


Figure 8. Baseline and controlled 4/Rev hub loads obtained using closed-loop AFC at various advance ratios; results are nondimensional


*This work is licensed under the Creative Commons Attribution International License (CC BY). Copyright © 2021 by author(s).*

At low advance ratios ($\mu < 0.30$), the 5/Rev harmonic is the second largest component of the signal. This is somewhat unexpected, since the control sensitivity matrices indicated that vibratory loads are relatively insensitive to 5/Rev actuation (Fig. 7). Therefore, the 5/Rev harmonic is likely only needed to satisfy the saturation limit constraint. The contribution of the 3/Rev harmonic is only significant when $\mu = 0.35$. This is necessary to reduce the higher in-plane vibratory loads generated by dynamic stall.

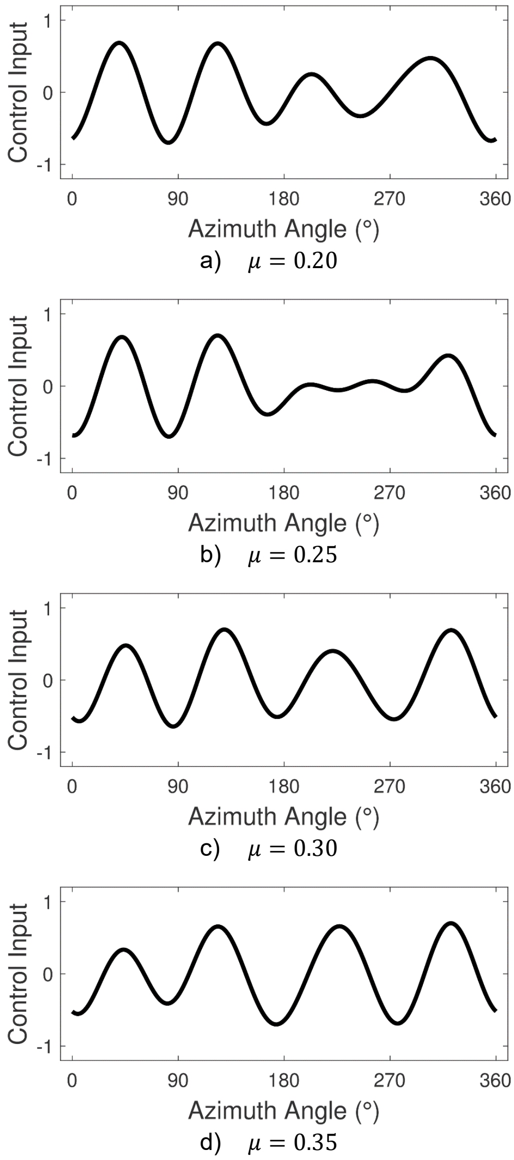


Figure 9. AFC control input signals computed by HHC algorithm for closed-loop vibration reduction at various advance ratios

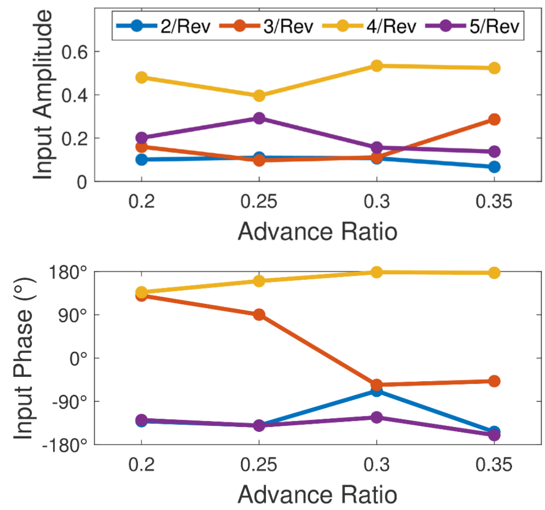


Figure 10. Amplitude and phase of 2, 3, 4, and 5/Rev harmonics computed by HHC algorithm for closed-loop vibration reduction using AFC at various advance ratios

Figure 11 illustrates the rotor performance penalty associated with active vibration reduction. Figure 11a shows the overall change in the vibration objective, which is a combination of all the 4/Rev hub load components. The power increment, shown in Fig. 11b, is calculated as a percentage of the baseline power required to overcome in-plane drag forces on the rotor without AFC. Note that the baseline conditions are different for each advance ratio. The baseline power required increases with $\mu$, since the rotor must produce an increasing level of forward thrust. Therefore, the power increment is calculated relative to the baseline conditions at each advance ratio.

The level of vibration reduction is consistent across the range of advance ratios, varying between 70% and 80% below the baseline. The power increment, however, increases rapidly from 2.5% to 8.8% as the advance ratio increases from $\mu = 0.20$ to $\mu = 0.35$. The performance penalty is due to the in-plane drag induced by AFC. As $\mu$ increases, the mean effective angle of attack on the rotor blades increases. This is indicated by the collective pitch setting required for trim (Fig. 6). The amplitude of the 1/Rev angle of attack variations also increases, as indicated by the cyclic pitch settings required for trim. Furthermore, when AFC is employed at high angles of attack, the drag penalty due to actuation increases significantly.


*This work is licensed under the Creative Commons Attribution International License (CC BY). Copyright © 2021 by author(s).*

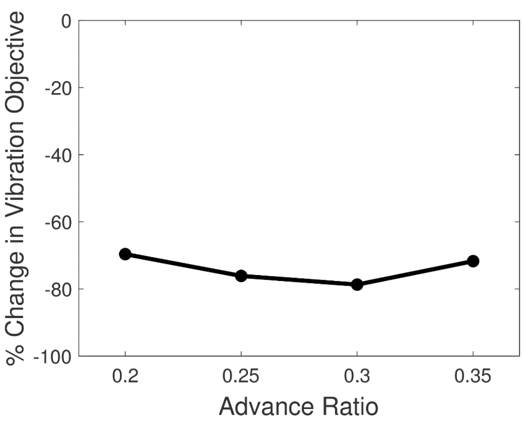


a) Vibration reduction

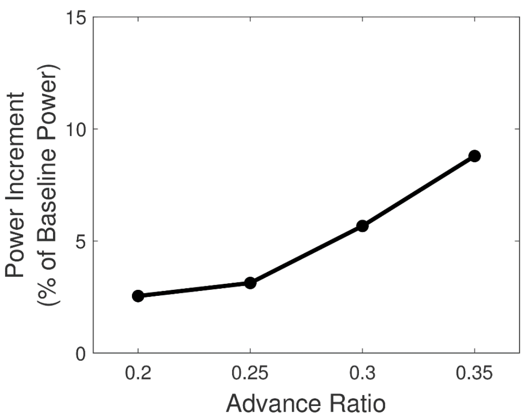


b) Performance penalty

Figure 11. Vibration reduction and associated performance penalty using closed-loop AFC at various advance ratios

## 6. CONCLUSIONS

The vibration reduction capability of active flow control was demonstrated using aeroelastic simulations of a helicopter in forward flight operating at advance ratios in the range of $0.20 \leq \mu \leq 0.35$. The closed-loop control approach was based on the HHC algorithm and used an optimization-based approach to handle actuator saturation constraints. The control sensitivity matrix $\mathbf{T}$ used in the HHC algorithm was examined, to gain insight into the types of control signals that are most effective for vibration reduction. The performance penalty associated with reducing vibrations was also examined. The main conclusions from this study are:

1. The entries of the control sensitivity matrix $\mathbf{T}$ vary significantly depending on the rotor advance ratio. The 4/Rev in-plane hub shear forces are most sensitive to 3/Rev actuation and become more sensitive as $\mu$ increases. The 4/Rev vertical hub shear force is most sensitive to 4/Rev actuation at low advance ratios but becomes more sensitive to 3/Rev actuation at higher advance ratios where dynamic stall is present.
2. The closed-loop AFC approach is effective for reducing vibrations at all advance ratios considered ($0.20 \leq \mu \leq 0.35$). The 4/Rev vertical shear was reduced by more than 80% in all cases. The reduction of the 4/Rev in-plane shears improved with increasing advance ratio, indicating that the adverse effects of dynamic stall were alleviated.
3. Although the overall level of vibration reduction was consistent around 70% to 80% across the range of advance ratios, the associated performance penalty increases with increasing advance ratio, due to higher drag penalty associated with fluidic actuation.

The simulations performed in this study have provided further evidence that AFC is a potentially viable method for reducing rotor blade vibrations. Furthermore, the simulations have demonstrated the ability of the closed-loop control approach to reduce vibrations under a variety of different flow conditions, including dynamic stall.


## ACKNOWLEDGMENTS

This research was partially funded by the Government under Agreement No. W911W6-17-2-0002. The U.S. Government is authorized to reproduce and distribute reprints for Government purposes notwithstanding any copyright notation thereon. The views and conclusions contained in this document are those of the authors and should not be interpreted as representing the official policies, either expressed or implied, of the U.S. Army Aviation Development Directorate, CCDC AvMC.


## REFERENCES


[1] Friedmann, P. P., "On-Blade Control of Rotor Vibration, Noise, and Performance: Just Around the Corner? The 33rd Alexander Nikolsky Honorary Lecture," *Journal of the American Helicopter Society*, Vol. 59, (4), October 2014, pp. 1-37.

[2] Patt, D., Liu, L., and Friedmann, P. P., "Rotorcraft Vibration Reduction and Noise Prediction Using a Unified Aeroelastic Response Simulation," *Journal of the American Helicopter Society*, Vol. 50, (1), January 2005, pp. 95–106.

[3] Patt, D., Liu, L., and Friedmann, P. P., "Simultaneous Vibration and Noise Reduction in Rotorcraft Using Aeroelastic Simulation," *Journal of the American Helicopter Society*, Vol. 51, (2), April 2006, pp. 127–140.

[4] Ravichandran, K., Chopra, I.,Wake, B. E., and Hein, B., "Trailing-Edge Flaps for Rotor Performance Enhancement and Vibration Reduction,"



*This work is licensed under the Creative Commons Attribution International License (CC BY). Copyright © 2021 by author(s).*

*Journal of the American Helicopter Society*, Vol. 58, (2), April 2013, pp. 1–13.

[5] Roget, B., and Chopra, I., “Wind-Tunnel Testing of Rotor with Individually Controlled Trailing-Edge Flaps for Vibration Reduction,” *Journal of Aircraft*, Vol. 45, (3), May 2008, pp. 868–879.

[6] Straub, F. K., Anand, V. R., Lau, B. H., and Birchette, T. S., “Wind Tunnel Test of the SMART Active Flap Rotor,” *Journal of the American Helicopter Society*, Vol. 63, (1), January 2018, pp. 1–16.

[7] Rabourdin, A., Maurice, J., Dieterich, O., and Konstanzer, P., “Blue Pulse Active Rotor Control at Airbus Helicopters – New EC145 Demonstrator and Flight Test Results,” *70th Annual Forum of the American Helicopter Society*, Montréal, Canada, 20-22 May, 2014.

[8] Matalanis, C. G., Wake, B. E., Opoku, D., Min, B.-Y., Yeshala, N., and Sankar, L., “Aerodynamic Evaluation of Miniature Trailing-Edge Effectors for Active Rotor Control,” *Journal of Aircraft*, Vol. 48, (3), May 2011, pp. 995–1004.

[9] Liu, L., Padthe, A. K., and Friedmann, P. P., “Computational Study of Microflaps with Application to Vibration Reduction in Helicopter Rotors,” *AIAA Journal*, Vol. 49, (7), July 2011, pp. 1450–1465.

[10] Padthe, A. K., and Friedmann, P. P., “Simultaneous Blade-Vortex Interaction Noise and Vibration Reduction in Rotorcraft Using Microflaps, Including the Effect of Actuator Saturation,” *Journal of the American Helicopter Society*, Vol. 60, (4), October 2015, pp. 1-16.

[11] Min, B.-Y., Sankar, L. N., and Bauchau, O. A., “A CFD–CSD coupled-analysis of HART-II rotor vibration reduction using gurney flaps,” *Aerospace Science and Technology*, Vol. 48, January 2016, pp. 308–321.

[12] Patterson, R. P., and Friedmann, P. P., “Computational Simulations of Fluidic Actuation on Rotor Blades and Their Experimental Validation,” *Journal of Aircraft*, published online 17 May 2021.

[13] Tan, Y., and Glezer, A., “Transitory, Bi-Directional Control of the Aerodynamic Loads on an Airfoil,” *AIAA SciTech 2020 Forum*, AIAA Paper 2020-0823, Orlando, FL, 6-10 January, 2020.

[14] Tan, Y., and Glezer, A., “Controlled Aerodynamic Loads at Low Angles of Attack using Fluidic Actuation,” *AIAA Scitech 2019 Forum*, AIAA Paper 2019-0889, San Diego, CA, 7-11 January, 2019.

[15] Patterson, R. P., and Friedmann, P. P., “Vibration Reduction on Helicopter Rotors Using Open Loop Flow Control,” *AIAA SciTech 2021 Forum*, AIAA Paper 2021-0089, Virtual Event, 11-21 January, 2021.

[16] Patterson, R. P., and Friedmann, P. P., “Vibration Reduction in Rotorcraft Using Closed-Loop Active Flow Control,” *77th Annual Forum of the Vertical Flight Society*, Virtual Event, 10-14 May, 2021.

[17] Patt, D., Liu, L., Chandrasekar, J., Bernstein, D. S., and Friedmann, P. P., “Higher-Harmonic-Control Algorithm for Helicopter Vibration Reduction Revisited,” *Journal of Guidance, Control, and Dynamics*, Vol. 28, (5), September 2005, pp. 918–930.

[18] Cribbs, R., and Friedmann, P., “Actuator Saturation and Its Influence on Vibration Reduction by Actively Controlled Flaps,” *42nd AIAA/ASME/ASCE/AHS/ACS Structures, Structural Dynamics, and Materials Conference*, AIAA Paper 2001-1467, Seattle, WA, 16-19 April, 2001.

[19] Roget, B., and Chopra, I., “Closed-Loop Test of a Rotor with Individually Controlled Trailing-Edge Flaps for Vibration Reduction,” *Journal of the American Helicopter Society*, Vol. 55, (1), January 2010, pp. 1–12.

[20] Chakravarthy, S., Peroomian, O., Goldberg, U., and Palaniswamy, S., “The CFD++ Computational Fluid Dynamics Software Suite,” *AIAA and SAE, 1998 World Aviation Conference*, AIAA Paper 1998-5564, Anaheim, CA, 28-30 September, 1998.

[21] Forrester, A., Sóbester, A., and Keane, A., *Engineering Design via Surrogate Modeling: A Practical Guide*, AIAA, Reston, VA, 2008.

[22] Glaz, B., Friedmann, P., Liu, L., Kumar, D., and Cesnik, C., “The AVINOR Aeroelastic Simulation Code and Its Application to Reduced Vibration Composite Rotor Blade Design,” *50th AIAA/ASME/ASCE/AHS/ASC Structures, Structural Dynamics, and Materials Conference*, AIAA Paper 2009-2601, Palm Springs, CA, 4-7 May, 2009.

[23] Padthe, A., *Active Noise and Vibration Alleviation in Rotorcraft Using Microflaps*, Ph.D. thesis, University of Michigan, 2011.

Presented at 47th European Rotorcraft Forum, United Kingdom, 7-9th September, 2021.
*This work is licensed under the Creative Commons Attribution International License (CC BY). Copyright © 2021 by author(s).* 